Chinese Chemical Letters 35 (2024) 108601

Contents lists available at ScienceDirect

Chinese Chemical Letters

journal homepage: www.elsevier.com/locate/cclet

Hybridization chain reaction-based DNA nanomaterials for biosensing, bioimaging and therapeutics

Zhaoyue Lv[a,1], Mengxue Huang[a,1], Peiran Li[a], Mengdi Xu[a], Chi Yao[a,b,*], Dayong Yang[a,b,*]

[a] Frontiers Science Center for Synthetic Biology, Key Laboratory of Systems Bioengineering (MOE), Institute of Biomolecular and Biomedical Engineering, School of Chemical Engineering and Technology, Tianjin University, Tianjin 300350, China
[b] Zhejiang Institute of Tianjin University, Ningbo 315201, China

ARTICLE INFO

Article history:
Received 5 March 2023
Revised 19 May 2023
Accepted 22 May 2023
Available online 24 May 2023

Keywords:
DNA nanotechnology
Hybridization chain reaction
DNA nanomaterials
Biosensing
Bioimaging
Therapeutics

ABSTRACT

DNA nanomaterials hold great promise in biomedical fields due to its excellent sequence programmability, molecular recognition ability and biocompatibility. Hybridization chain reaction (HCR) is a simple and efficient isothermal enzyme-free amplification strategy of DNA, generating nicked double helices with repeated units. Through the design of HCR hairpins, multiple nanomaterials with desired functions are assembled by DNA, exhibiting great potential in biomedical applications. Herein, the recent progress of HCR-based DNA nanomaterials for biosensing, bioimaging and therapeutics are summarized. Representative works are exemplified to demonstrate how HCR-based DNA nanomaterials are designed and constructed. The challenges and prospects of the development of HCR-based DNA nanomaterials are discussed. We envision that rationally designing HCR-based DNA nanomaterials will facilitate the development of biomedical applications.

1. Introduction

DNA is traditionally known as a genetic biomacromolecule in life systems [1]. From the perspective of materials chemistry, DNA has emerged as a promising versatile building-block for construction multiple materials due to its unique sequence programmability, and precise molecular recognition capability and biocompatibility [2]. Hybridization chain reaction (HCR) is an isothermal amplification strategy of DNA, which produces nicked double helices with repeat modules *via* cascade assembly of two hairpin monomers [3]. Owing to its enzyme-free nature, simple reaction process and excellent amplification efficiency, HCR provides a powerful molecular tool to design and construct HCR-based DNA nanomaterials [4].

HCR, first proposed by Dirks and Pierce in 2004, is an isothermal enzyme-free amplification strategy with mild reaction process [3]. A typical HCR system contains an initiator (termed as I) and at least two hairpins (termed as H1 and H2) [5]. The hairpin is composed of three domains: stem, loop, and toehold. When the hairpin forms secondary structure, the long stem is complementary to the short, storing potential energy in the complementary bases [6]. In the absence of initiator, the two hairpins are metastable and coexist stably. Whereas, in the presence of the initiator I (a'-b'), I recognizes the toehold domain (a) of hairpin H1 and binds to the long stem (a-b) of H1 *via* a toehold-mediated strand displacement (TMSD) reaction, thereby exposing the loop region (c) and short stem (b') of H1. Afterwards, the loop region (c) of H1 recognizes the toehold domain (c') of hairpin H2 and binds to its long stem (c'-b), exposing loop region (a') and short stem (b') of H2. With the alternating combination of hairpins H1 and H2, long-stranded DNA with sticky ends is eventually formed until one hairpin is exhausted (Fig. 1) [7]. The kinetics of HCR has been determined to be controlled by the length and types of bases in toehold domain [8]. If the toehold domain is too short, HCR will not be effectively triggered. Equally if the toehold region is too long, the secondary structure of hairpin will be unstable and prone to self-opening, thus risking signal leakage. It has been demonstrated that when the toehold length is about 6–10 nucleotides, hairpins can be opened effectively and the reaction rate of HCR remains sta-

* Corresponding authors at: Frontiers Science Center for Synthetic Biology, Key Laboratory of Systems Bioengineering (MOE), Institute of Biomolecular and Biomedical Engineering, School of Chemical Engineering and Technology, Tianjin University, Tianjin 300350, China.
E-mail addresses: chi.yao@tju.edu.cn (C. Yao), dayong.yang@tju.edu.cn (D. Yang).
[1] These authors contributed equally to this work.

https://doi.org/10.1016/j.cclet.2023.108601
1001-8417/

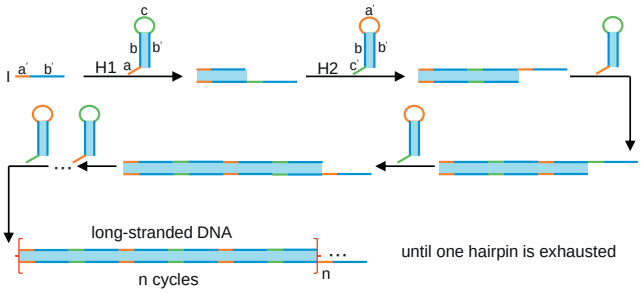

Fig. 1. Schematic illustration of the process of hybridization chain reaction (HCR).

ble [9]. Moreover, the high GC content in the stem of hairpin can effectively stabilize its structure and prevent background leakage [5]. The length of the formed dsDNA is affected by the molar ratio of initiator to hairpin and the reaction time [10]. In general, the larger molar ratio is, the shorter the length of DNA strands is; in the presence of sufficient hairpin, the longer the reaction time, the longer the length of DNA strands. In addition, the appropriate concentration of Mg^{2+} facilitates the stability of the formed DNA strands [11]. Therefore, the size of HCR products can be generally regulated.

Through rational design of HCR hairpins, HCR-based DNA nanomaterials with specific and desired biological functions are rationally designed and constructed [12–14]. Target-triggered HCR could amplify an output signal over hundreds of times, which decreases the detection limit of targets in biosensing assays [15]. For example, Zhang *et al.* constructed an HCR-based photoelectrochemical (PEC) sensing system, which showed high sensitivity toward carcinoembryonic antigen (CEA) with a dynamic range of 0.02–40 ng/mL and a detection limit of 5.2 pg/mL [16]. Further, coupling florescent groups with HCR could convert target molecule signals into visualized florescent signals, enhancing the efficiency of bioimaging *via* accumulation of florescent signals [17]. By modifying fluorescent groups on HCR hairpins, Zhang *et al.* constructed an enhanced HCR probe system with fluorescence resonance energy transfer (FRET) effect for tumor site-specific imaging [18]. Jiang *et al.* designed a two-dimensional HCR nanosystem, which achieved simultaneously amplified sensing and imaging of intracellular mRNA [19]. In addition, by virtue of tandem DNA double helixes yielded by HCR, molecular drugs (doxorubicin) were successfully loaded, enabling target cancer cell apoptosis with the assistance of aptamer-tethered initiator [20]. In particular, different functional DNA sequences such as small interfering RNA (siRNA) and DNAzyme can be programmed and integrated to HCR products [6,21–23]. By designing the sequence of HCR hairpins, the spherical nucleic acid-templated hydrogel with ATP responsive and tumor targeting ability was constructed, realizing burst release of payloads [13].

In this review, the recent advances in the design, construction, and biomedical applications including biosensing, bioimaging and therapeutics of HCR-based DNA nanomaterials are summarized and discussed in detail. Finally, the challenges and future opportunities of HCR-based DNA nanomaterials are discussed and prospected.

2. HCR-based DNA nanomaterials for biosensing

HCR is an important technique that is used in many DNA-based biosensing systems. Through HCR, functional moieties such as nanoparticles and electrochemical reagents could be incorporated in HCR products, which applied HCR-based DNA nanomaterials in biosensing and signal transduction with high sensitivity [24–26]. The signal amplified by HCR can be used for qualitative analysis of targets and sensitive detection of various targets, including mRNA, proteins and metal ions [27]. A comparison of different HCR-based DNA nanomaterials for biosensing is listed in Table 1.

Aptamers are short oligonucleotide sequences, which possess high specificity recognition and binding affinity to cognate targets [28]. Gao *et al.* developed an HCR-based colorimetric aptasensor, which realized determination of small molecule ATP by coupling visible-colored gold nanoparticles (AuNPs) with two hairpin probes (H1 and H2) [29]. In the absence of target ATP, the toehold of two hairpin probes prevented AuNPs from salt-induced aggregation *via* the interaction between ssDNA at the sticky end and AuNPs; while in the presence of target ATP, hairpin H1 containing ATP aptamer was opened to expose a new sticky end for the strand displacement reaction of hairpin H2, generating long DNA strands and resulting in decrease of ssDNA to cause AuNPs aggregated upon addition of salt (Fig. 2A). The diameter of AuNPs increased from 15.8 ± 0.3 nm to 376.4 ± 12.6 nm, inducing a blue shift of local surface plasmon resonance (LSPR) peak of gold colloids. Meanwhile, the color of resulting solution changed from red to bluish. With the concentration of ATP increased from 10 nmol/L to 600 nmol/L, an increase in absorbance at 630 nm and a decrease at 520 nm were observed. A good linear relationship between the absorbance and ATP concentrations was achieved, and the limit of detection (LOD) was 1.0 nmol/L (Fig. 2B). After incubation of ATP and ATP analogues (CTP, GTP and UTP), the aptasensor showed a new shift in the SPR peak only in the presence of target ATP, indicating the high selectivity and specificity of HCR-based colorimetric aptasensor. Designing the sequence of can determine different targets. Nevertheless, the assay process and reaction time needs to be improved.

Multiplex analysis of biomarkers is essential and of great use for clinical diagnosis [30]. Jiang *et al.* designed OR and AND gates based on DNA-templated silver nanoclusters (AgNCs) and HCR for simultaneous detection and analysis of telomerase activity and miRNA [31]. The biomarkers in including telomerase and miRNA that need to be detected as the input [32,33]. AgNCs were synthesized in the presence of DNA template sequence of hairpin H2 at 3′ end, which emitted fluorescence as the output. After hairpins H1 and H2 being adsorbed on the surface of graphene oxide (GO), the red emit of AgNCs in H2 was quenched *via* FRET. For the OR gate, $H0_{OR}$ was released in the presence of telomerase or miRNA, which further triggered cascade HCR of H1 and H2 to recover and enrich fluorescence. For the AND gate, the downstream HCR was successfully initiated for the subsequent fluorescence output in the presence of inputs telomerase and miRNA (Fig. 2C). The LOD of OR gate for miRNA was calculated to be 2.8 pmol/L (S/N = 3), and telomerase was calculated to be 2 cells (S/N = 3), respectively. Fluorescence emission spectra of OR gate showed that fluorescence was

Table 1
Summary of HCR-based DNA nanomaterials for biosensing.

Carrier	Target	Method	Signal transduction	Detection limit	Ref.
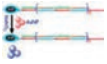	ATP	ATP aptamers bind to ATP preferentially over AuNPs	Absorbance	1.0 nmol/L ATP	[29]
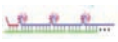	miRNA/telomerase	Interactions between AgNPs and graphene oxide (GO)	Fluorescence	2.8 pmol/L (miRNA)/2 cells (Telomerase)	[31]

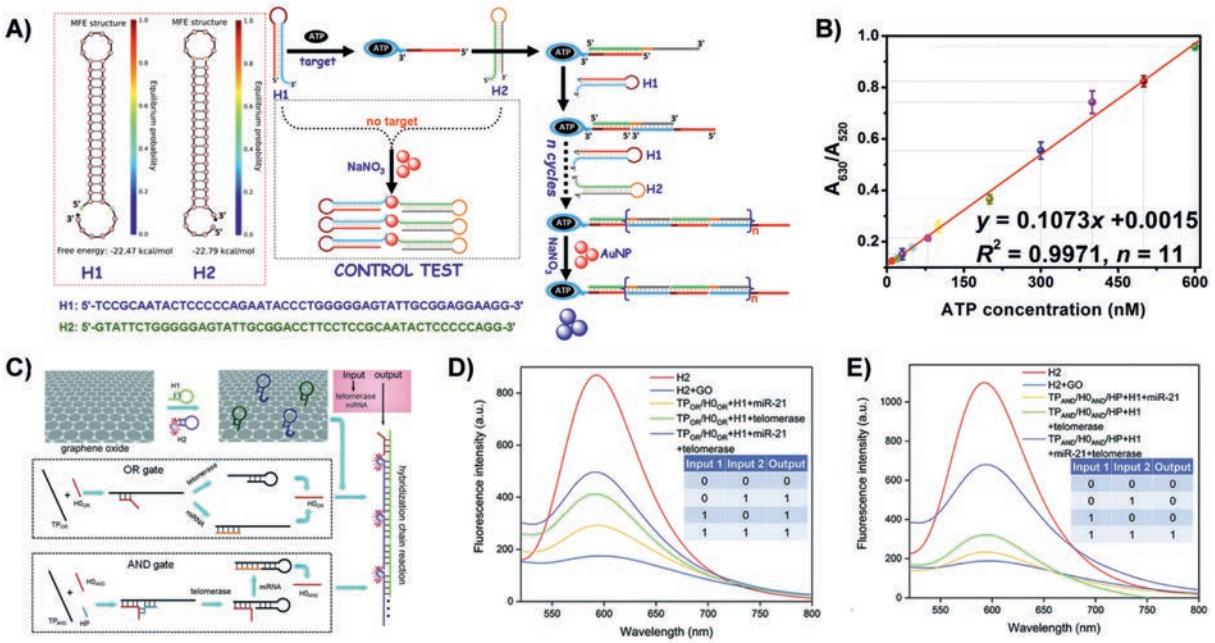

Fig. 2. HCR-based DNA nanomaterials for biosensing. (A) The molecular design of HCR-based colorimetric aptasensor. (B) Calibration diagram for ATP concentration *vs.* absorbance ratio (A_{630}/A_{520}). Copied with permission [29]. Copyright 2017, Elsevier Publishing Group. (C) The molecular design of AgNCs and HCR-based logic gates responding to miRNA and telomerase. Fluorescence emission spectra of OR gate (D) and AND gate (E) in the presence of various inputs. Copied with permission [31]. Copyright 2022, Royal Society of Chemistry.

quenched in the absence of two inputs, and fluorescence was recovered with single input alone. While fluorescence emission spectra of AND gate showed that significant fluorescence recovery after simultaneously inputting the two targets (Figs. 2D and E). To sum up, the AgNCs and HCR based fluorescence system possessed excellent selectivity. This logic gates were simple and sensitivity to operate, and was applied for intracellular imaging.

3. HCR-based DNA nanomaterials for bioimaging

Bioimaging, especially for cellular fluorescence imaging, has the advantage of visible biological distribution and real-time information feedback, thus it is essential for disease detection and early biosensing [34]. However, the intensity of cellular single fluorescence signals is often weak for imaging molecules with low concentrations. Therefore, signal amplification strategies are needed to combine with the actual imaging process to amplify the signal and achieve accurate imaging of trace substances [35]. By modifying fluorescent groups in hairpins, HCR-based DNA nanomaterials could enrich fluorescent signals during the process of HCR, which provides more possibilities for bioimaging [36]. In addition, the initiator sequence of HCR could be designed to be same as the sequence of intracellular target molecule, enabling HCR-based DNA nanomaterials to perform specific imaging functions, and thus to facilitate disease assessment [37]. A comparison of different HCR-based nanomaterials for bioimaging is listed in Table 2.

Nucleic acid-based systems are programmable for molecular imaging, but there is still a strong requirement for aptamer sensing systems with high sensitivity, accuracy, and adaptability for *in vivo* imaging. Wu *et al.* designed a multilayer HCR aptasensing system for *in situ* imaging of biomolecule [38]. The HCR aptasensing circuit consisted of two sections including HCR-I and HCR-II circuit. In HCR-I circuit, an aptamer/initiator-encoded strand (IA) had the initial recognition region of biomolecule, which was efficiently hybridized with a blocker strand (Inh). Once the target molecule was recognized, the initiator in IA was exposed with the release of Inh, facilitating the formation of HCR-I circuit by

Table 2
Summary of HCR-based DNA nanomaterials for bioimaging.

Carrier	Particle size	Target	Signal transduction	Cell type	*In vivo* effect	Ref.
	/	miRNA-21	Fluorescence	MCF-7 cells	Yes	[38]
	40 nm	c-MYC	Fluorescence	MCF-7 cells	Yes	[39]
	155 nm	ATP	Fluorescence	MCF-7 cells	Yes	[42]

H1 and H2. The initiator is *in situ* translated by HCR-I circuit to generate long stranded DNA that carried numerous tandemly triggers of HCR-II circuit. Each of HCR-II triggers simultaneously initiated the following fluorophore donor/acceptor-bearing HCR-II circuit leading to remarkable fluorescence readout. The HCR aptasensing circuit encapsulated by a folic acid-modified poly(D,L-lactic-*co*-glycolic acid) (FA-PLGA) nanocarrier was selectively released in the cytoplasm of tumor cells, which achieved generated a "turn-on" fluorescence output with an utmost 2 × N_2-fold amplification efficiency (Fig. 3A). The fluorescence intensity of FAM in Hela cells co-treated with IA/Inh and HCRs hairpins was comparable to those cells co-treated with single IA strands and HCRs hairpins, while the fluorescence intensity of was greatly decreased when either initiator or one of the hairpins was absent (Fig. 3B). Fluorescence images of HeLa tumor-bearing mice and corresponding statistics showed that the HCRs/FP system was enabled to target molecular imaging with high spatial selectivity (Figs. 3C and D). The *ex vivo* fluorescence imaging results of the major organs showed that the Cy5 signals were mainly accumulated in liver, kidney, and tumor. Therefore, the HCRs/FP system provided a powerful tool for tracing bioactive molecule *in vivo* (Figs. 3E and F).

Spatiotemporally controlled signal amplification provides unparalleled opportunities for bioimaging. Chu *et al.* developed a

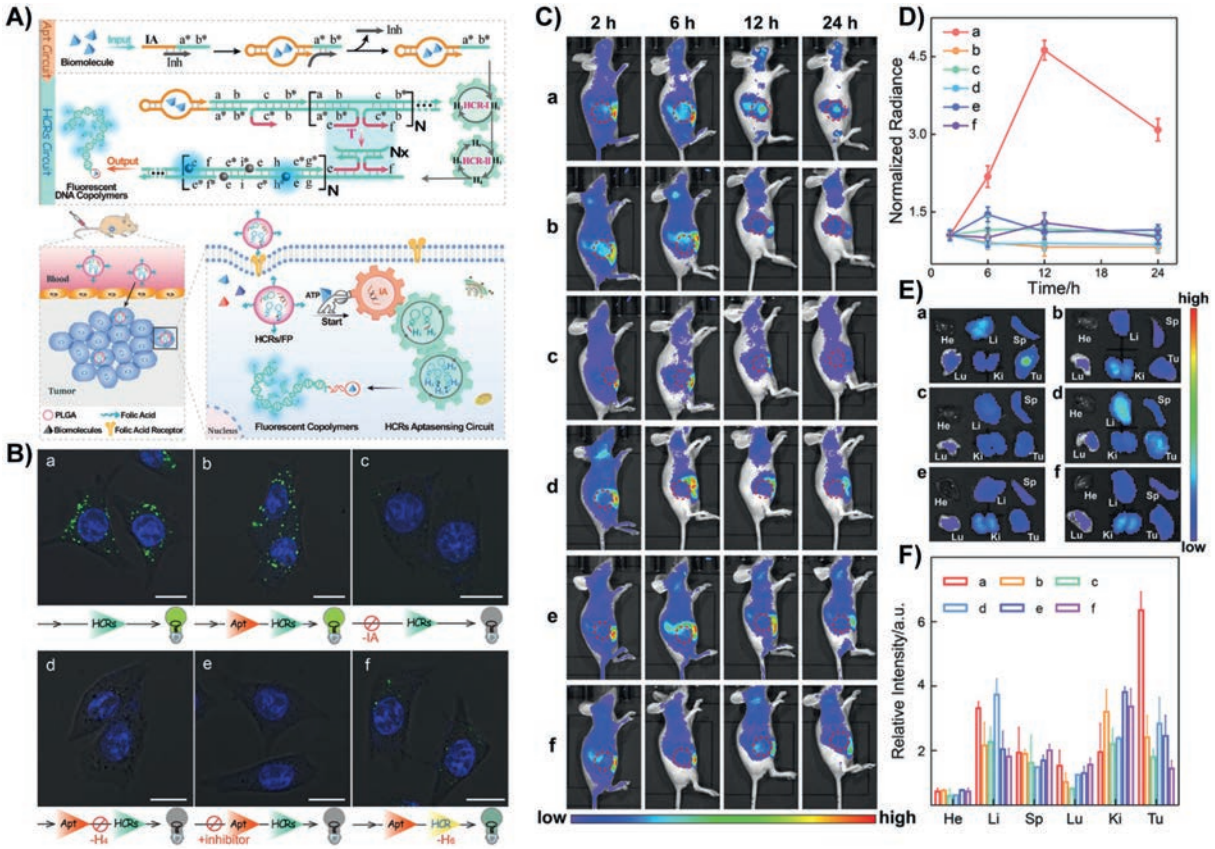

Fig. 3. HCR-based DNA nanomaterial for biomolecule imaging *in vivo*. (A) The molecular design and preparation of HCR/FPs for bioimaging. (B) Confocal laser scanning microscope (CLSM) images of ATP in living HeLa cells with different treatments. (a) single IA strand and HCRs circuit, (b) HCRs aptasensing circuit, (c) Inh strand and HCRs, (d) H4-expelled HCRs aptasensing circuit, (e) HCRs aptasensing circuit with oligomycin, and (f) conventional HCR aptasensing circuit. Scale bars:15 μm. (C) Whole-body fluorescence imaging of HeLa tumor-bearing mice after intravenous injection with different treatments. (a) HCR/FPs system, (b) IA/Inh-expelled HCR/FPs system, (c) HCR/FPs system after 3-bromopyruvic acid-pretreatment, (d) H4-expelled HCR/FPs system, (e) H6-expelled HCR/FPs system, and (f) HCRs/PLGA system without folic acid moiety. (D) Mean F.L. intensity statistics of tumor sites in (C). (E) *Ex vivo* imaging of major organs and tumor of mice with different treatments at 24 h post intravenous injection. He = heart; Lu = lung; Li = liver; Ki = kidney; Tu = tumor; Sp = spleen. (F) Mean F.L. intensity statistics of major organs and tumor (E). Data are represented as mean ± S.D., $n = 3$. Copied with permission [38]. Copyright 2022, Wiley Publishing Group.

near-infrared (NIR) lightNIR-initiated HCR for spatiotemporally controlled signal amplification, which achieved imaging of messenger RNA (mRNA) with ultrahigh sensitivity *in vitro* and *in vivo* [39]. Lanthanide-ion-doped upconversion nanoparticles (UCNPs) not only served as photoconverters to convert NIR to UV, but also served as carriers to deliver hairpins into cells. The 5′ end of H1 was added a six-base sequence *via* a photocleavable (PC) linker to form PH1. UV irradiation induced photolysis of the PC linker in PH1 to generate a toehold in cleaved PH1(H1), which facilitated the initiator-induced HCR. H1 was labeled with Cy3 fluorophores and H2 was labeled with Cy5 fluorophores. Through HCR initiated by intracellular target molecule mRNA, the donor (Cy3) fluorescence significantly decreased, while the acceptor (Cy5) fluorescence increased, showing the efficient production of FRET signal (Fig. 4A). Due to the expression level of target molecule mRNA in different cells, varying FRET signals were observed (Fig. 4B). NIR light effectively penetrated deep tissues and activated HCR-based precise imaging of mRNA in tumor tissues. Therefore, the HCR activated by UCNPs for FRET-based fluorescence imaging was promising for a wide range in the field of spatiotemporal controlled amplification imaging of target molecules.

DNAzyme is a DNA molecule with catalytic functions for specifically recognizing and catalyzing the cleavage of target mRNA [40,41]. As an effective transducer for visualizing endogenous biomarkers, DNAzyme is limited for clinical application due to the insufficient supply of DNAzyme cofactors. Wei *et al.* constructed an autocatalytic DNAzyme (ACD) biocircuit sustained by honeycomb MnO_2 nanosponge (hMNS) based on HCR and DNAzyme biocatalysis for *in vivo* miRNA imaging [42]. Upon the uptake by cells, hMNS was responded to intracellular GSH, inducing the conversion of MnO_2 to Mn^{2+} that served as DNAzyme cofactors and magnetic resonance imaging (MRI) agents. DNA probes included hairpins H1, H2, H3 and H4, and DNAzyme substrate hybrids (S/L). Both H1 and H3 contained DNAzyme subunits. H2 was modified with an acceptor and H4 was modified with a donor. After HCR was initiated by target miRNA, the DNAzyme subunits of H1 and H3 linked together to constitute an active DNAzyme. With additional Mn^{2+}, the cleavage efficiency of DNAzyme was increased and S/L was cleaved by DNAzyme to release multiple initiators, thus back-feeding the initiation of multiple HCR. Furthermore, the acceptor of H2 and the donor of H4 leaded to effective FRET during HCR, achieving precise imaging of target molecules based on the fluorescence intensity ratio (Fig. 4C). Confocal laser scanning microscope (CLSM) images showed that the fluorescence intensity of hMNS/ACD imaged in different cells was consistent to the actual content of intracellular target molecules, and the imaging fluorescence intensity of hMNS/ACD was significantly greater than that of the hMNS/HCR (HCR instead of ACD system) (Figs. 4D and E). *In vivo* experiments also indicated that hMNS/ACD had enhanced signal amplification and precise target molecule imaging abilities (Figs. 4F-H). In addition, high MRI signals were also acquired in the tumor region, demonstrating that hMNS/ACD had dual imaging functions of flu-

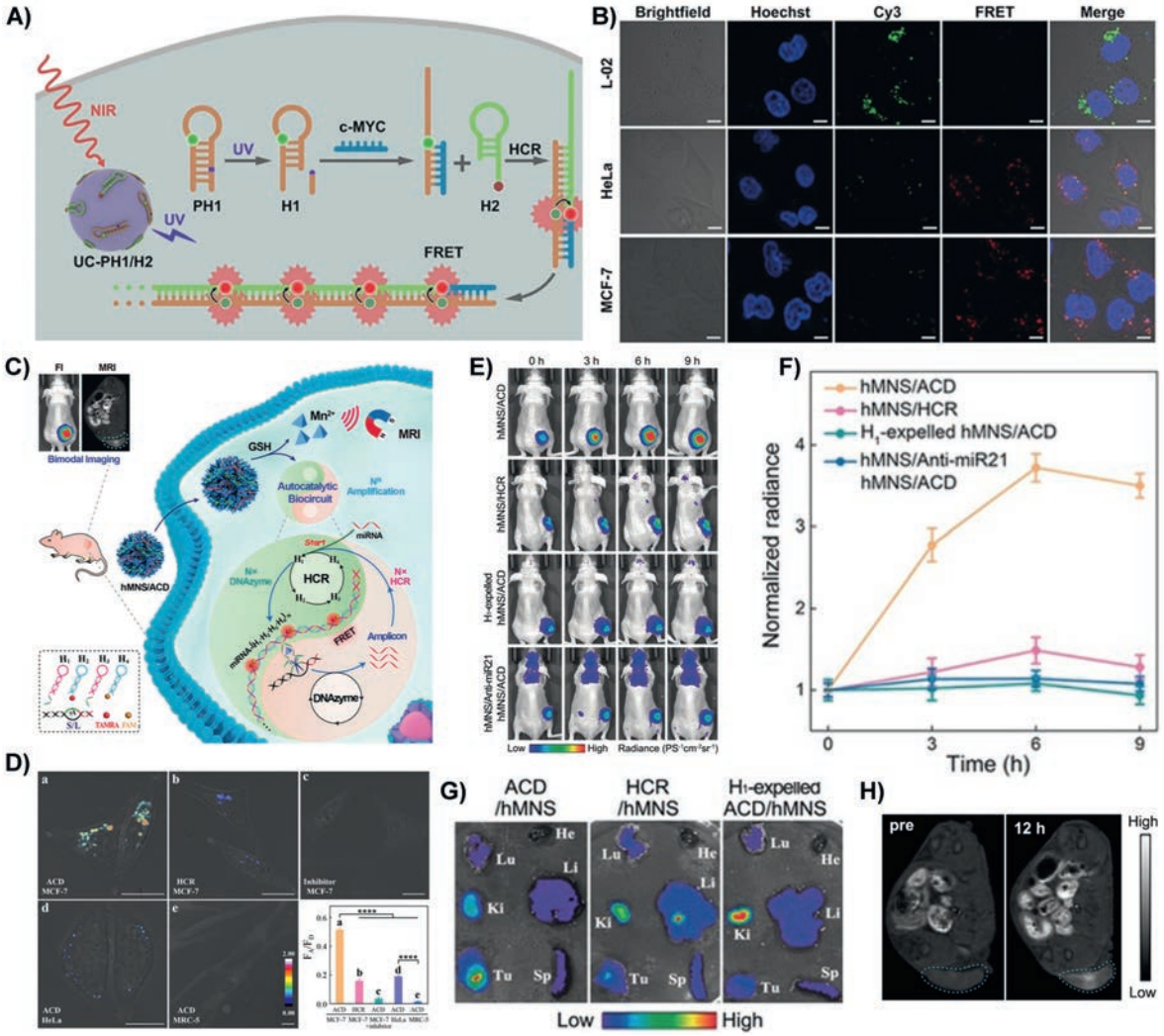

Fig. 4. HCR-based DNA nanomaterial for bioimaging *via* sensitized fluorescence. (A) The molecular design and preparation of NIR-light-initiated HCR for spatiotemporally imaging of mRNA with signal amplification. (B) CLSM images of different cells treated with UC-PH1/H2 and NIR irradiation. Scale bars: 10 μm. Copied with permission [39]. Copyright 2019, Wiley Publishing Group. (C) The molecular design and preparation of hMNS-sustained autocatalytic DNAzyme biocircuit for amplified miR-21 imaging. (D) CLSM images of miR-21 imaging in various cells with different treatments and corresponding statistical analysis of fluorescence resonance energy transfer (FRET)-based ratiometric fluorescence. Scale bars: 20 μm. (E) Whole-body fluorescence imaging of MCF-7-tumor-bearing mice after intravenous injection with different treatments. (F) Mean F.L. intensity statistics of tumor sites in (E). (G) *Ex vivo* imaging of major organs and tumor of mice after intravenous injection 12 h with different treatments. (He = heart; Lu = lung; Li = liver; Ki = kidney; Tu = tumor; Sp = spleen). (H) *In vivo* MR images of mice bearing MCF-7 tumor before and after intravenous injection of hMNS/ACD. The circles indicated tumor sites. Copied with permission [42]. Copyright 2020, Wiley Publishing Group.

orescence and MR, which was significant for clinical diagnosis and therapeutic evaluation.

4. HCR-based DNA nanomaterials for therapeutics

Through rational design of initiator as well as hairpins, HCR-based DNA nanomaterials can be programmed with functional units such as therapeutic sequences (siRNA, miRNA, ASOs and DNAzyme), and stimuli-responsive motifs (i-motif and G-quadruplex), holding great promise in therapeutics [21,43]. In particular, the unique sequence programmability of DNA endows HCR-based DNA nanomaterials with dynamic assembly property, which could affect cellular behaviors such as cell proliferation, migration, and differentiation to modulate cell fates and promote diseases treatment [44,45]. A comparison of different HCR-based nanomaterials for therapeutics is listed in Table 3. siRNA is a nucleic acid drug with precise and efficient gene silencing effects, which is widely applied in therapeutics [46]. The gene silencing efficiency of siRNA is greatly depended on the level of cellular uptake and cytoplasm release. Li *et al.* constructed a DNA cross-linked polymeric nanoframework (DPNF) for precise siRNA delivery, which significantly suppressed tumor growth [47]. The DPNF was prepared *via* precipitation copolymerization of NIPAM, 4-MAPBA, Bis, and Acrydite-DNA, in which Acrydite-DNA served as the initiator for HCR. The 3′ end of hairpin H2 was designed with ATP aptamer that was tethered with siRNA *via* base pairing. Upon exposure to the initiator DNA, hairpins H1 and H2 was alternatively bond to each other, achieving efficient loading of siRNA to form DPNF-siRNA. The high ATP level in tumor cells enabled release of siRNA from DPNF-siRNA for gene therapy (Fig. 5A). The ATP responsive release of siRNA was verified by FRET effect. FRET is a non-radiative energy leap that transfers the energy from the excited state of the donor to the excited state of the acceptor through intermolecular electric dipole interactions, causing the donor to fluoresce less intensely, while the acceptor can either emit a fluorescence stronger than itself (sensitized fluorescence) or not (fluorescence quench) [48–51]. The hairpin H2 was modified with a fluorescent label (Cy5, donor) and the ssDNA (instead of siRNA) was modified with a quencher (BHQ2, acceptor). The quenched fluorescence of Cy5 was recovered when ssDNA was dissolved from hairpin H2. Fluorescence mi-

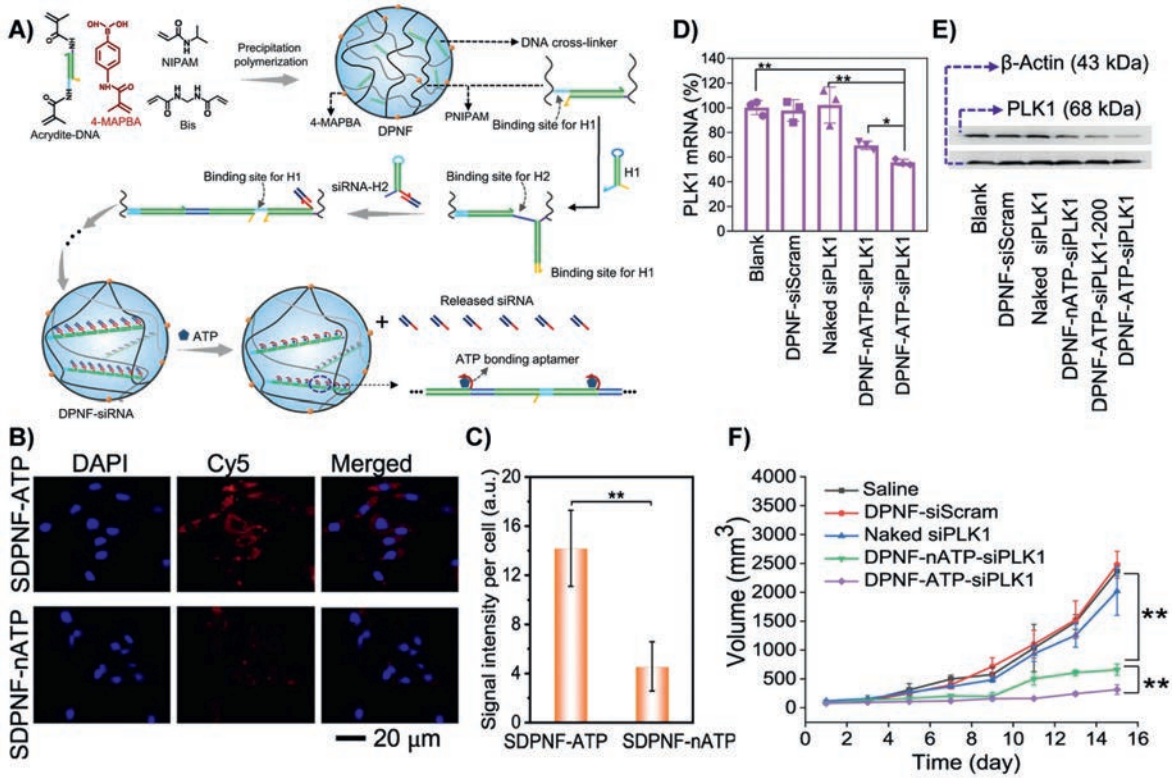

Fig. 5. HCR-based DNA nanomaterial for gene therapy. (A) The molecular design and preparation of DPNF-siRNA and ATP-driven release of siRNA. (B) CLSM images of MDA-MB-231 cells treated with SDPNF-ATP and SDPNF-nATP, respectively (SDPNF was prepared by dsDNA instead of siRNA). (C) Mean fluorescence (F.L.) intensity statistics of per cell in (B). Data are represented as mean ± S.D., $n = 20$. $^{**}P < 0.01$. (D) RT-qPCR analysis of PLK1 mRNA levels in the MBA-MD-231 cells with different treatments. Data are represented as mean ± S.D., $n = 3$. $^{*}P < 0.05$, $^{**}P < 0.01$. (E) Western blotting (WB) analysis of PLK1 expression in MBA-MD-231 cells with different treatments. (F) Tumor growth curves from the different treated mice. $^{**}P < 0.01$. Copied with permission [47]. Copyright 2021, Springer Nature.

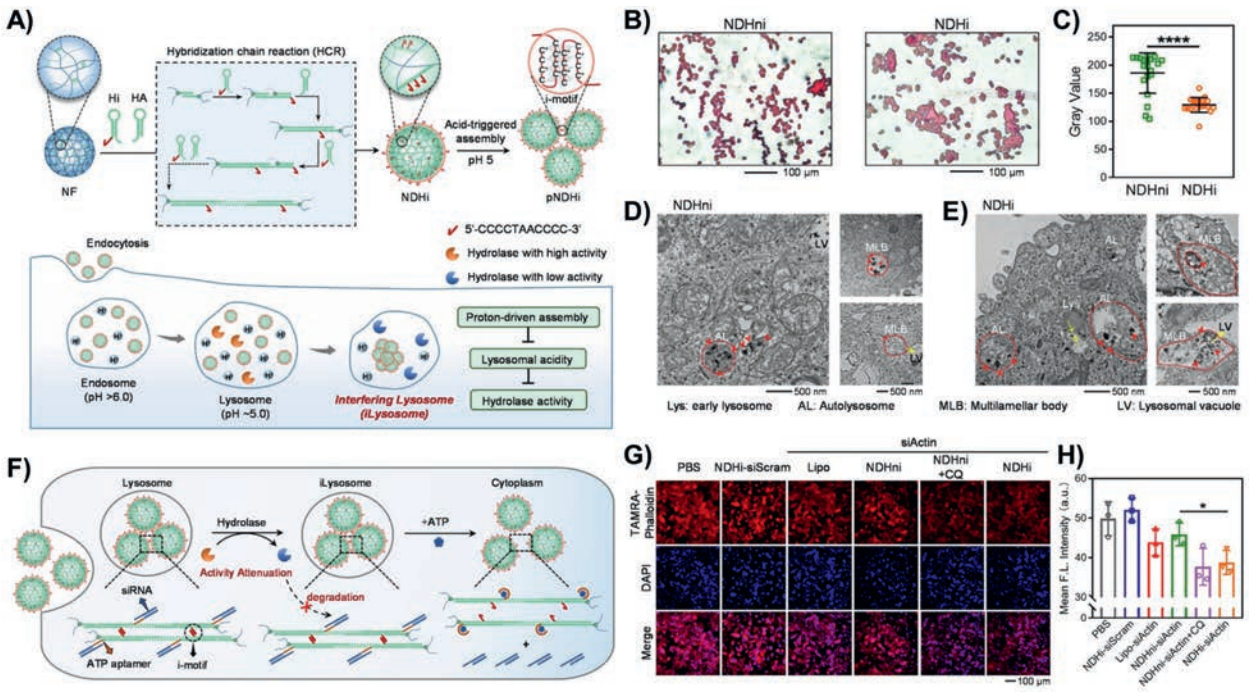

Fig. 6. HCR-based DNA nanomaterial for lysosome interference and gene therapy. (A) The molecular design and preparation of NDHi for lysosome interference and gene therapy. (B) TRAP staining images of cells treated with NDHni and NDHi, respectively. (C) Gray value statistics of TRAP staining in (B). Data are represented as mean ± S.D., $n = 20$. $^{****}P < 0.0001$. (D, E) Bio-TEM images of cells treated with NDHni and NDHi, respectively. The red arrows represented NDs. The yellow arrows showed the possible movement direction of vesicles and vesicle fusion. (F) Schematic illustration of ATP-driven release of siRNA from siRNA-loading NDHi. (G) Fluorescence images of β-actin in cells treated with different treatments. (H) Mean F.L. intensity statistics of β-actin in (G). Data are represented as mean ± S.D., $n = 3$. $^{*}P < 0.05$. Copied with permission [54]. Copyright 2022, Wiley Publishing Group.

Table 3
Summary of HCR-based DNA nanomaterials for therapeutics

Carrier	Particle size	Responsive sequence	Gene agents	Synergistic therapies	Cell type	*In vivo* effect	Ref.
	180 nm	ATP aptamer	siRNA	/	MBA-MD-231 cells	Yes	[47]
	220 nm	ATP aptamer, i-motif	siRNA	/	A549 cells	No	[54]
	220 nm	ATP aptamer	siRNA	Chemical regulation	MCF-7 cells	Yes	[56]

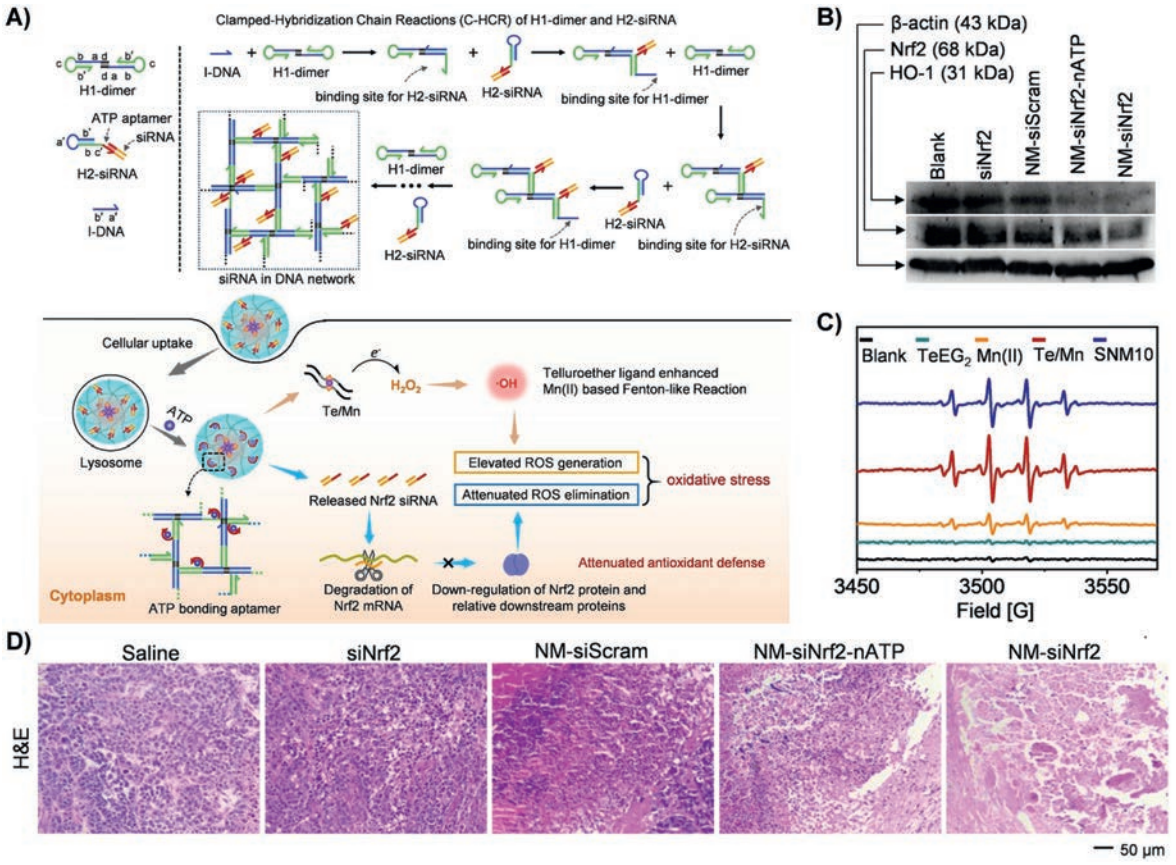

Fig. 7. HCR-based DNA nanomaterial for synergistic chemodynamic therapy and gene therapy. (A) The molecular design and preparation of NM-siNrf2 for the co-delivery of Te/Mn coordination complex and siNrf2. (B) WB analysis of Nrf2 and HO-1 expression in MCF-7 cells with different treatments. (C) Electron spin resonance (ESR) spectra of different samples in the presence of H_2O_2. (D) H&E staining of tumor tissue collected from the different treated mice. Copied with permission [56]. Copyright 2022, Wiley Publishing Group.

croscopy images showed that the fluorescence intensity of Cy5 in SDPNF-ATP group (ssDNA linked with ATP aptamer) was about 3.5 times greater than that of SDPNF-nATP group (ssDNA linked with non-ATP aptamer), indicating that ATP-responsive property facilitated the release of siRNA (Figs. 5B and C). RT-qPCR and western blotting (WB) analysis showed that the mRNA and protein expression levels of PLK1 were significantly decreased in DPNF-siRNA treated group, indicating that DPNF-siRNA possessed effective gene silencing effect (Figs. 5D and E). For *in vivo* experiments, DPNF-siRNA had significant anti-tumor effects, demonstrating that the smart HCR-based DNA nanomaterial were emerging as a precise platform for disease treatment (Fig. 5F).

The combination of material chemistry systems and biological processes effectively modulates organelle function, thereby interfering with therapeutic effects. i-motif is a stimulus-responsive sequence, and it folds to form a four-stranded structure by protonation of cytosine under acidic conditions and deprotonates under non-acidic conditions [52,53]. Dong *et al.* reported an HCR-based DNA nanoframework (NDHi)containing i-motif sequences to achieve proton-driven dynamic assembly, interfering with lysosomal function and thus enabling gene therapy [54]. The hairpin Hi was designed with semi-i-motif sequence at the 5′ end, and two hairpins Hi could form C-quadruplexes under acid condition. Through HCR, multiple semi-i-motif sequences were integrated in the DNA crosslinked nanoframework (NF), generating an HCR-based nanomaterial (NDHi). In the acidic environment of lysosome, NDHi with semi-i-motif sequences were aggregated due to the formation of a complete i-motif structure, decreasing lysosomal acidity and hydrolase activity to achieve lysosome interference (Fig. 6A). Tartrate-resistant acid phosphatase (TRAP) was a lysosomal hydrolase to obtain activity under acidic environment. Compared to NDHni with scramble i-motif sequences treated group,

the level of TRAP activity in NDHi-treated group was significantly decreased, indicating that proton-driven assembly weakened hydrolase activity (Figs. 6B and C). The degradation of NDHi was greatly inhibited with the decrease of hydrolase activity the degradation of substances (Figs. 6D and E), which would prevent nucleic acid drugs from nuclease degradation. Actin siRNA was tethered on hairpin HA and was released in response to ATP (Fig. 6F). Fluorescence images and corresponding statistical values showed that the fluorescence intensity of actin in NDHi-treated cells was weaker than that of in NDHni-treated cells, indicating that lysosomal dysfunction enhanced the gene silencing efficiency of siRNA, and thus contributed to gene therapy (Figs. 6G and H).

Targeted construction of therapeutic systems based on the characteristics of cells is an essential strategy for precision medicine. Cancer cells possess high redox capacity compared to normal cells, which are thus more susceptible to oxidative stress induced by excessive reactive oxygen species (ROS) [55]. Li *et al.* constructed a supramolecular self-assembled DNA nanosystem (NM-siNrf2) based on cascade clamped hybridization chain reaction (C-HCR) to enhance intracellular oxidative stress though synergistic chemodynamic and gene modulation, thereby significantly inhibiting tumor progression [56]. The Te/Mn coordination complex and cholesterol-modified initiator DNA were co-assembled to from nanomicelles (NM). In a C-HCR, hairpin H1 with a palindromic segment at 5′ end could form a hairpin-dimer (H1-dimer) *via* base pairing; Hairpin H2 was designed with ATP aptamer at 3′ end of H2. In the presence of initiator DNA assembled on NMs, H1-dimer and H2-siRNA alternately hybridized with each other to form a DNA network, which was released to Nrf2 siRNA (siNrf2) in response to ATP for ROS elimination and catalyzed with H_2O_2 for ROS generation. Under the synergistic of siRNA-mediated gene silencing and MnII-mediated chemodynamic reaction, NM- siNrf2 enabled oxidative stress to achieve efficient tumor suppression. (Fig. 7A). WB analysis demonstrated that the expression of Nrf2 and its downstream protein HO-1 were significantly decreased, indicating that NM-siNrf2 had efficient gene silencing effect (Fig. 7B). Electron spin resonance (ESR) spectra showed that Te/Mn coordination complex enhanced the Fenton-like catalytic capability of Mn^{II} to convert H_2O_2 to $^{\bullet}OH$, increasing intracellular ROS levels (Fig. 7C). The synergistic chemodynamic- and gene-therapeutic effect was verified in H&E-stained tumor tissues, which showed that NF-siNrf2 greatly induced tumor cell apoptosis and thus inhibited tumor progression (Fig. 7D).

5. Conclusion

In this review, we have summarized the design principles and synthesis methods of HCR, and the biological applications of HCR-based DNA nanomaterials, mainly including biosensing, bioimaging and therapeutics.

Owing to excellent sequence programmability and molecular recognition ability of DNA, DNA-based nanomaterials can be constructed with specific and desired functions, which hold great potential in biomedical applications. As an efficient enzyme-free amplification platform, HCR provides a powerful tool to design and construct HCR-based nanomaterials to be applied in the fields of biosensing, bioimaging and therapeutics. Through the rational design of initiator and hairpin of HCR system, HCR-based DNA nanomaterials can be efficiently loaded with multiple nucleic acid drugs and responded to endogenous stimuli such as ATP, pH, metal ions to control the release of drugs, facilitating the therapeutic effect. In addition, HCR-based DNA nanomaterials have exceptional properties including biocompatibility and biodegradability, making them arouse great interests in bioimaging. Moreover, HCR-based DNA nanomaterials are mainly for fluorescence imaging, and fluorescence signal amplification can be achieved through HCR process, which is beneficial to the decrease of detection limit and the enhancement of imaging sensitivity.

Although HCR-based DNA nanomaterials have been widely used for biosensing, bioimaging and therapeutics, challenges remain to be considered. (1) The design of HCR-based DNA nanomaterials with multi-responsive units and more diversified functions to biosensing, bioimaging and therapeutics is desire but challenging, elaborately design of the hairpins from linear to nonlinear HCR can be considered. (2) Although design guidelines based on simulation experiments were proposed for the design of length and CG content of stem and toehold domains in hairpins, there is still a lack of design system guidelines for designing hairpin sequences [5]. (3) Delivery of HCR-based nanomaterials into targeted cells for biosensing, bioimaging and therapeutics needs to be considered. Reprogramming specific DNA aptamers to endow HCR-based nanomaterials with tumor targeting ability should be considered. (4) As exogenous substance, the immunogenic effects and metabolic pathways of DNA nanomaterials are still unclear *in vivo*, and the metabolism of HCR products needed further explored [57]. (5) The preparation cost of HCR-based DNA nanomaterials needs to be considered. Developing and optimizing the synthesis methods and techniques of DNA nanomaterials from small-scale laboratory synthesis to large-scale practical applications should be considered.

With the development of DNA nanotechnology and HCR-based isothermal amplification techniques, we envision that HCR-based DNA nanomaterials with more diversity and functions will give more possibility of biomedical fields, especially for biosensing, bioimaging and therapeutics [58,59].

Declaration of competing interest

The authors declare that they have no known competing financial interests or personal relationships that could have appeared to influence the work reported in this paper.

Acknowledgment

This work was supported in part by National Natural Science Foundation of China (Nos. 22225505, 22174097).

References

[1] N.C. Seeman, H.F. Sleiman, Nat. Rev. Mater. 3 (2018) 17068.
[2] D. Yang, M.R. Hartman, T.L. Derrien, et al., Acc. Chem. Res. 47 (2014) 1902–1911.
[3] R.M. Dirks, N.A. Pierce, Proc. Natl. Acad. Sci. U. S. A. 101 (2004) 15275–15278.
[4] F.C. Simmel, B. Yurke, H.R. Singh, Chem. Rev. 119 (2019) 6326–6369.
[5] Y.S. Ang, L.Y.L. Yung, Chem. Commun. 52 (2016) 4219–4222.
[6] J. Zhuang, L. Fu, M. Xu, et al., Biosens. Bioelectron. 45 (2013) 52–57.
[7] Q. Zhou, Y. Lin, Y. Lin, et al., Talanta 146 (2016) 23–28.
[8] D.Y. Zhang, E. Winfree, J. Am. Chem. Soc. 131 (2009) 17303–17314.
[9] S. Li, P. Li, M. Ge, et al., Nucleic Acids Res. 48 (2020) 2220–2231.
[10] H. Chai, W. Cheng, D. Jin, P. Miao, ACS Appl. Mater. Interfaces 13 (2021) 38931–38946.
[11] X. Zhou, X. Liu, X. Xia, X. Yang, H. Xiang, J. Electroanal. Chem. 870 (2020) 114270.
[12] J. Zhang, M. Hou, G. Chen, et al., Chin. Chem. Lett. 32 (2021) 3474–3478.
[13] Z. Chen, W.T. Wang, W. Wang, et al., ACS Appl. Mater. Interfaces 14 (2022) 44054–44064.
[14] J. Chen, H. Xue, Q. Chen, et al., Chin. Chem. Lett. 30 (2019) 1631–1634.
[15] R. Zeng, L. Zhang, L. Su, et al., Biosens. Bioelectron. 133 (2019) 100–106.
[16] K. Zhang, S. Lv, Q. Zhou, D. Tang, Sens. Actuators B: Chem. 307 (2020) 127631.
[17] H.M.C. Choi, J.Y. Chang, L.A. Trinh, et al., Nat. Biotechnol. 28 (2010) 1208–1212.
[18] B. Zhang, T. Tian, D. Xiao, et al., Adv. Funct. Mater. 32 (2022) 2109728.
[19] P. Miao, Y. Tang, Anal. Chem. 92 (2020) 12700–12709.
[20] G. Zhu, J. Zheng, E. Song, et al., Proc. Natl. Acad. Sci. U. S. A. 110 (2013) 7998–8003.
[21] X. Gong, H. Wang, R. Li, et al., Nat. Commun. 12 (2021) 3953.
[22] Y. Xue, H. Xie, Y. Wang, et al., Biosens. Bioelectron. 218 (2022) 114762.
[23] J. Wei, H. Wang, X. Gong, et al., Nucleic Acids Res. 48 (2020) e60.
[24] J. Kim, J.S. Shim, B.H. Han, et al., Biosens. Bioelectron. 192 (2021) 113504.
[25] N. Li, J. Chen, M. Luo, et al., Biosens. Bioelectron. 87 (2017) 325–331.
[26] Z. Huang, J. Chen, Z. Luo, X. Wang, Y. Duan, Anal. Chem. 91 (2019) 4806–4813.
[27] S. Bi, S. Yue, S. Zhang, Chem. Soc. Rev. 46 (2017) 4281–4298.

[28] H. Yu, O. Alkhamis, J. Canoura, Y. Liu, Y. Xiao, Angew. Chem. Int. Ed. 60 (2021) 16800–16823.
[29] Z. Gao, Z. Qiu, M. Lu, J. Shu, D. Tang, Biosens. Bioelectron. 89 (2017) 1006–1012.
[30] L. Yang, X. Yin, B. An, F. Li, Anal. Chem. 93 (2021) 1709–1716.
[31] Y. Jiang, Z. Guo, M. Wang, J. Cui, P. Miao, Nanoscale 14 (2022) 612–616.
[32] X. Zhou, D. Xing, Chem. Soc. Rev. 41 (2012) 4643–4656.
[33] J. Ge, Y. Hu, R. Deng, et al., Anal. Chem. 92 (2020) 13588–13594.
[34] Y. Xu, Z. Lv, C. Yao, D. Yang, Biomater. Sci. 10 (2022) 3054–3061.
[35] B.N.G. Giepmans, S.R. Adams, M.H. Ellisman, R.Y. Tsien, Science 312 (2006) 217–224.
[36] J. Shang, J. Wei, Q. Wang, et al., Biosens. Bioelectron. 152 (2020) 111994.
[37] S. Zada, H. Lu, W. Dai, et al., Biosens. Bioelectron. 197 (2022) 113815.
[38] Q. Wu, L. Yang, L. Xie, et al., Small 18 (2022) 2200983.
[39] H. Chu, J. Zhao, Y. Mi, Y. Zhao, L. Li, Angew. Chem. Int. Ed. 58 (2019) 14877–14881.
[40] C. Yao, H. Qi, X. Jia, et al., Angew. Chem. Int. Ed. 61 (2022) e202113619.
[41] H. Zhao, Z. Zhang, D. Zuo, et al., Nano Lett. 21 (2021) 5377–5385.
[42] J. Wei, H. Wang, Q. Wu, et al., Angew. Chem. Int. Ed. 59 (2020) 5965–5971.
[43] C.H. Lu, B. Willner, I. Willner, ACS Nano 7 (2013) 8320–8332.
[44] C. Yao, Y. Xu, J. Tang, et al., Nat. Commun. 13 (2022) 7739.
[45] F. Li, Y. Liu, Y. Dong, et al., J. Am. Chem. Soc. 144 (2022) 4667–4677.
[46] D. Castanotto, J.J. Rossi, Nature 457 (2009) 426–433.
[47] F. Li, W. Yu, J. Zhang, et al., Nat. Commun. 12 (2021) 1138.
[48] D.K. Sasmal, L.E. Pulido, S. Kasal, J. Huang, Nanoscale 8 (2016) 19928–19944.
[49] W.A. Velema, W. Szymanski, B.L. Feringa, J. Am. Chem. Soc. 136 (2014) 2178–2191.
[50] X. Tao, Z. Liao, Y. Zhang, et al., Chin. Chem. Lett. 32 (2021) 791–795.
[51] A.T. Blanchard, Z. Li, E.C. Duran, et al., Nano Lett. 22 (2022) 6235–6244.
[52] M. Debnath, K. Fatma, J. Dash, Angew. Chem. Int. Ed. 58 (2019) 2942–2957.
[53] Y. Dong, Z. Yang, D. Liu, Acc. Chem. Res. 47 (2014) 1853–1860.
[54] Y. Dong, F. Li, Z. Lv, et al., Angew. Chem. Int. Ed. 61 (2022) e202207770.
[55] B. Kwon, E. Han, W. Yang, et al., ACS Appl. Mater. Interfaces 8 (2016) 5887–5897.
[56] F. Li, Z. Lv, X. Zhang, et al., Angew. Chem. Int. Ed. 60 (2021) 25557–25566.
[57] S. Surana, A.R. Shenoy, Y. Krishnan, Nat. Nanotechnol. 10 (2015) 741–747.
[58] Y. Dong, C. Yao, Y. Zhu, et al., Chem. Rev. 120 (2020) 9420–9481.
[59] F. Wang, C.H. Lu, I. Willner, Chem. Rev. 114 (2014) 2881–2941.